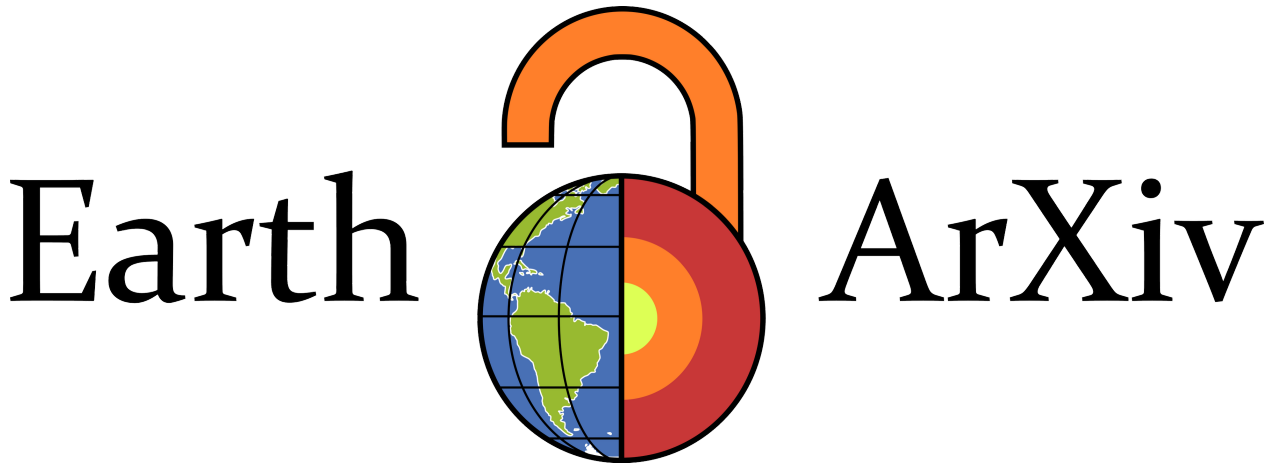

SWOT Satellite Altimetry Observations and Source Model for the Tsunami from the 2025 M8.8 Kamchatka Earthquake

A. Ruiz-Angulo[1,*], D. Melgar[2], Charly de Marez[3] ,Deniau Aurélien[4], and Francesco Nencioli[4] ,Vala Hjörleifsdóttir[5]

[1] *Institute of Earth Sciences, University of Iceland, Reykjavik, Iceland*

[2] *Department of Earth Sciences, University of Oregon, Eugene, OR, USA*

[3] *Univ Brest, CNRS, Laboratoire d'Océanographie Physique et Spatiale (LOPS), IUEM, Plouzané, France*

[4] *Collecte Localisation Satellites (CLS), Ramonville St Agne, France*

[5] *Reykjavík University, Reykjavik, Iceland*

[*]Corresponding author: angel@hi.is

ABSTRACT

On 29 July 2025 a Mw 8.8 earthquake struck off Kamchatka, Russia generating a Pacific-wide tsunami and marking the largest earthquake since the launch of the SWOT satellite in 2022. We analyze tsunami observations from SWOT together with three nearby DART buoys to resolve the source of the event. SWOT provided the first high-resolution spaceborne track of a great subduction-zone tsunami, capturing waveforms that reveal complex propagation, dispersion, and scattering. Inversion of DART time series using Gaussian unit sources shows that the rupture extended ~400 km along strike, with peak uplift of ~4 m, significantly different from published finite-fault model. A blended source that combines the DART-inverted uplift with subsidence from the seismic–geodetic model best matches both datasets and reproduces the SWOT observations. Comparison with reconstructions of the 1952 Mw 9.0 Kamchatka earthquake indicates that the 2025 rupture likely re-activated significant portions of the megathrust that broke in 1952 but occurred farther

downdip and with little to no near-trench slip, consistent with its smaller tsunami impact. These findings highlight the hazard implications of short recurrence intervals of great earthquakes and show how rupture style governs tsunami severity. They also demonstrate the value of satellite altimetry for improving tsunami source characterization, post-event forecasting, and understanding of hydrodynamic processes.

OVERVIEW AND IMPACTS OF THE EVENT

On July 29th, 2025, a M8.8 earthquake struck off the coast of the Kamchatka Peninsula (Figure 1), marking the sixth largest earthquake ever recorded globally since 1900 (Wirth, Sahakian, et al., 2022). The rupture occurred along the Kuril–Kamchatka subduction zone, where the Pacific Plate dives beneath the North American Plate at ~8 cm/yr (Prytkov et al., 2017), one of the fastest convergence rates on Earth (Argus et al., 2011), and where cold, dense oceanic lithosphere is driven steeply into the mantle (Koulakov et al., 2011). This highly coupled plate interface (Burgmann et al., 2005; Prytkov et al., 2017) has produced numerous great megathrust ruptures, making it one of the most seismically and tsunamigenic active margins in the world. For example, the 1952 M9.0 event (Hutchinson, 1954; Johnson & Satake, 1999; MacInnes et al., 2010), produced one of the largest recorded Pacific tsunamis (Kaistrenko & Sedaeva, 2001). That event was pivotal in advancing tsunami science and spurred the creation of modern warning systems, laying the groundwork for the international monitoring and communication networks that responded to the 2025 tsunami.

This most recent earthquake also generated a significant tsunami that was detected by tide gauges and deep-ocean instruments across the entire Pacific basin, from Russia to South America. Tsunami warnings and advisories were issued for much of the Pacific Rim, prompting coastal evacuations and emergency response actions throughout the region.

In this paper, we present a novel set of observations of the 2025 tsunami from the Surface Water and Ocean Topography (SWOT) satellite altimeter (Morrow et al., 2019), offering an unprecedentedly dense space-based measurement of tsunami propagation at high resolution; this event is the largest magnitude recorded since the launch of SWOT in 2022. Here, we compare the SWOT-derived signals to deep-ocean pressure gauge data from the Deep-Ocean Assessment and Reporting of Tsunamis (DART) buoy system to assess their consistency and potential for rapid hazard characterization and for understanding tsunami hydrodynamics. Using the DART observations, we also produce an inversion for the tsunami source and compare the resulting seafloor deformation model against available coseismic slip inversions derived from seismic and geodetic data. We show that the M8.8 source must extend further to the South, totaling a rupture length of ~400km, significantly longer than currently available slip models which suggest a rupture length of only ~300 km. Additionally, we compare the tsunami source to those produced by MacInnes et al. (2010) for the M9.0

1952 earthquake to understand whether the 2025 event represents re-rupturing of that portion of the megathrust.

The opportunity to capture such dense, high-resolution altimetric observations of a major tsunami, paired with independent source inversions, is exceptionally rare, providing unique insights into tsunami propagation, source characterization, and the future role of satellite measurements in operational warning systems, rapid response settings, as well as detailed analyses of both the earthquake and tsunami source.

TSUNAMI OBSERVATIONS, PROCESSING, AND MODELING METHODOLOGY

DART buoys

The DART system (Figure 1) is a global network of real-time tsunami monitoring stations operated primarily by NOAA and partner agencies (e.g. Mungov et al., 2013). Each DART consists of a bottom pressure recorder (BPR) deployed on the seafloor and a surface buoy moored directly above it. The BPR continuously measures the combined weight of the overlying water column, with changes in pressure recorded at sub-centimeter resolution, sensitive enough to detect tsunami wave amplitudes of just a few millimeters in the open ocean.

The BPR transmits its data acoustically to the surface buoy, which in turn relays the information via satellite to shore-based processing centers. Under normal conditions, DART stations transmit standard 15-minute data streams, but they automatically switch to “event mode” when anomalous pressure signals are detected, increasing the sampling rate to every 60 s or 15 s, depending on the size of the signal, to capture the tsunami waveform in detail.

For the 2025 Kamchatka tsunami, multiple DART stations across the North Pacific and beyond recorded the wave’s propagation, providing high-fidelity time series of wave arrival times, amplitudes, and dispersion characteristics. Here, we focus on three sites (Figure 1) closest to the tsunami source. It is noteworthy mentioning that this event has recorded one of the largest amplitudes of tsunami waves, 0.8 m, since the DART program started. The data are only lightly processed, because the waveforms have irregular sampling, we interpolate the observations to a regular 15 s sample rate and apply a high-pass filter with a 2 hr corner to remove the tides. This post-processed data is then used as the primary input to perform a

tsunami source inversion, estimating the seafloor deformation pattern that best explains the recorded waveforms.

Satellite Altimetry Observations from SWOT

We leverage observations of sea surface height data from the SWOT satellite program (a collaborative effort between NASA and CNES, Morrow et al., 2019), that observed with unprecedented details the propagation of the tsunami event resulting from the M8.8 Kamchatka earthquake. We employ the SWOT track from ascending pass #267 of the 36th cycle of the mission, from 2025-07-30 at 00:34 UTC to 2025-07-30 at 00:39 UTC (Figure 1).

We rely on the latest release (v2.0.1) of Level-3 SWOT data, namely the SWOT_L3_SSH 'Basic' (2-km resolution) product, derived from the L3 SWOT Ka-band Radar Interferometer, KaRIn, low-rate ocean data products provided by NASA/JPL and CNES. The Level-3 processing removes SWOT's systematic errors, which mainly corrects the roll/phase effects through crossover calibration, and does not contain the flagged data due to atmospheric perturbation. It has been extensively validated against other altimeters, numerical models, and in situ data in the global ocean (e.g. Dibarboure et al. 2025). For this analysis, we also make use of the SWOT altimeter, which is located at the center of the track. This dataset is produced and freely distributed by the AVISO and DUACS teams as part of the DESMOS Science Team project (AVISO/DUACS 2023). We use the "denoised" Sea Level Anomaly (SLA) for our analysis detailed by Dibarboure et al., (2023). Note that this process tends to reduce the overall energy, which complicates the interpretation in lower-energy regions due to the noise levels, but it should not affect observations of tsunami propagation given the high energy of this signal. The tsunami is significantly larger than the usual mesoscale dynamics the instrument is calibrated for. Recent studies have demonstrated that SWOT's resolution and noise level are sufficient to resolve features below this mesoscale, at the scales between 10-100 km (Tranchant et al. 2025, Coadou et al. 2025, Wang et al. 2025).

Earthquake Sources and Crustal Deformation

For the 2025 Kamchatka earthquake, we use the USGS finite-fault Version 3 source model (USGS, 2017) as the basis for our initial deformation calculations. This model incorporates a joint inversion of teleseismic body and surface waves together with InSAR-derived surface displacements, following the methodology of Goldberg et al. (2022). The combined dataset improves resolution of the slip distribution by leveraging the complementary strengths of

seismic and geodetic observations: teleseismic waveforms constrain the rupture timing and overall moment release, while InSAR provides high-spatial-resolution constraints on the near-field deformation pattern. The USGS V3 model represents the rupture on a discretized planar fault consistent with the Kuril–Kamchatka subduction interface geometry, with subfault slip, rake, rupture time, and rise time estimated by simulated annealing optimization.

To model the seafloor deformation associated with the rupture, we compute displacements assuming an elastic layered half-space representation of the Earth. The structure is parameterized using regional crustal properties derived from LITHO1.0, overlying a PREM mantle (Pasyanos et al., 2014), and accounts for realistic variations in seismic velocities and elastic moduli with depth. The resulting vertical deformation can be seen in Figure 2a,b, we use is as the initial condition for tsunami generation.

Direct inversion of DART buoys for the tsunami source

Because there are discrepancies (discussed later) between the predicted tsunami from the USGS source model and the DART observations we produced our own tsunami source estimate (Figure 2b,c). We inverted deep-ocean tsunami records from three DART buoys, 21415, 21416, and 21419 (Figure 1,3), to estimate the initial sea-surface displacement of the 2025 Kamchatka event. The inversion follows a "Gaussian lump" parameterization (e.g., Lin et al., 2020; Santellanes et al., 2025), in which the initial water surface is represented as a sum of localized Gaussian-shaped perturbations. Each Gaussian has a standard deviation of 15 km and is centered on a grid with 0.3° spacing in both latitude and longitude. This formulation allows for a smooth, spatially compact representation of the source while limiting the number of free parameters. A key advantage of this approach is that it makes no assumptions about the earthquake source geometry, rake, or slip distribution, allowing the tsunami data alone to determine the spatial pattern of initial displacement.

The inversion domain was restricted to a generous polygon surrounding the USGS Version 3 finite-fault source, ensuring the solution is physically consistent with independent seismic and geodetic constraints while allowing to explore deviations in source location or extent. To compute the tsunami Green's functions (GFs) for each Gaussian basis element, we used GeoClaw (Clawpack Development Team, 2024), a finite-volume numerical model that solves the nonlinear shallow-water equations (SWE) for wave propagation and inundation. For each

Gaussian, an initial sea-surface displacement was prescribed and propagated through the model to each DART location, producing unit-amplitude synthetic waveforms. The tsunami wavefield at the buoys is then represented as a linear combination of these precomputed Green's functions, with the inversion solving for the optimal coefficients of each Gaussian.

DART time series were band-pass filtered between 2 min and 2 hr to isolate as much as possible the tsunami band and suppress both high-frequency noise and long-period background signals (e.g., tides, infragravity waves). As it is usually the case, Rayleigh waves from the earthquake contaminate the earliest part of the DART pressure records, these surface waves generate vertical accelerations recorded as pressure fluctuations in the water column. To mitigate this effect and ensure linearity in the inversion, we manually picked the first clear wavelength of the tsunami signal for each buoy (yellow shaded regions in Figure 3c) and limited the inversion to that time window. This choice is further motivated by the fact that, while tsunami propagation is inherently nonlinear, a linear Green's function–based inversion can be valid when modeling is restricted to only the initial portion of the wave train before significant nonlinear interactions and dispersion occur (Melgar et al., 2013; Gusman et al., 2016).

The resulting inversion (Figure 2a,b) yields an initial sea-surface displacement field derived directly from tsunami observations, which we compare to the deformation predicted by the USGS V3 finite-fault model to evaluate consistency and identify possible differences in source characteristics.

Hydrodynamic Modeling to Match SWOT Observations

Using GeoClaw and our preferred initial condition model (Figure 2) we propagate the tsunami across the open ocean at high-resolution using the SRTM15+ global bathymetry data set (Tozer et al., 2019). As SWOT travels south to north along its polar orbit it samples the tsunami at different times, it is not a single snapshot at a fixed moment. Thus, to create a synthetic SWOT track we extract tsunami amplitudes from our simulations at the coordinates of each SWOT pixel at the appropriate time. To do so we generate output at over 60000 synthetic tide gauges and interpolate them to create a consistent synthetic product (Figures1,3b). Additionally, to try to reproduce as much of the wavefield captured by SWOT as possible we included dispersive wave dynamics from the Boussinesq-type solvers recently implemented in GeoClaw (Berger & LeVeque, 2023). These are based on the Serre–

Green–Naghdi (SGN) equations, a depth-averaged dispersive system that extends the standard SWE by including higher-order derivative terms. Adaptive mesh refinement is maintained by interpolating dispersive correction terms across refinement levels. In very shallow regions and onshore, the solver automatically reverts to SWE when the water depth falls below a prescribed threshold, ensuring robust inundation modeling. This hybrid approach allows GeoClaw to capture dispersion during tsunami propagation while maintaining computational efficiency and stability near shore.

RESULTS AND DISCUSSION

The tsunami source

The currently available best slip model for the event is the USGS V3 finite fault produced by joint inversion of tele-seismic and InSAR data. When we use it to initialize a hydrodynamic model (Figure 2a) and compare it to the DART observations (Figure 3e) we see its predicted waveforms arrive 3 and 10 mins early at DARTs 21415 and 21416 respectively, and 12 mins late at 21419. These are major discrepancies.

Meanwhile the Gaussian lump inversion corrects these large timing issues with ease. It is significantly different than the USGS source, it has much larger uplift in the southern 200 km and suggests that the extent of the earthquake is at least 400 km with a peak uplift of ~4 m at 51°N. There are some similarities though, with both the USGS V3 and Gaussian models showing a similar "down-dip" extent, the rupture terminates ~300 km landward of the trench.

We note, however, that, unlike the USGS V3 model, the Gaussian inversion has almost no subsidence, as would be expected for a pure thrust earthquake, which results in underestimating the negative pulse at 40 mins after OT at DART 21416. The USGS V3 model, despite its timing issues at all buoys, does a better job of replicating the amplitude of this negative pulse. For this reason, we produced a "blended" model (Figure 2c) which retains the positive/uplift portion of the Gaussian inversion and combines it with the negative/subsidence portion of the USGS V3 model. When we run the hydrodynamic propagation, we find that this blended source fits all three DART buoys to a similar degree as the Gaussian inversion (Figure 3c), with the added benefit of producing a more significant negative pulse at 21416. For this reason, we consider the blended model our "preferred" tsunami source.

Does 2025 re-rupture the portion of the megathrust involved in the M9 1952 event?

Most likely the 2025 earthquake re-ruptures significant portions of the megathrust that ruptured in 1952. This is also most likely limited to the down-dip portions of it. To establish this we studied the results of MacInnes et al. (2010) who extended the modeling work of Johnson and Satake (1999) and combined historical observations with 31 new tsunami-deposit surveys along Kamchatka and the northern Kuril Islands to reconstruct near-field runup from the 1952 earthquake. They then used the NOAA MOST model with different hypothetical slip distributions that included uniform, heterogeneous, and modified patterns, to simulate tsunamis and compare results against the expanded dataset. Their analysis showed that the best fits required concentrated, near-trench high-slip patches off southern Kamchatka and the northern Kurils. This indicates the 1952 rupture was heterogeneous, with significant slip extending closer to the trench than previously inferred. In Figure 2d we calculated the uplift/subsidence from the best fitting slip model from that work, labeled JASmod7 by the authors, against our preferred 2025 model. The along-strike extent is nearly identical, however the deformation from the 2025 earthquake locates further down-dip than in 1952 and involves no near-trench slip. This is consistent with 1952 having a much more damaging tsunami. Tantalizingly, our peak uplift is located almost exactly where between two high uplift patches from the 1952 earthquake. The large slip regions from JASmod7 from MacInnes et al. (2010) have 9-15 m of slip. At a convergence rate of 8 cm/yr only 5-6 m of slip could have reaccumulated since the 1952 rupture, so our results are a strong suggestion that the 1952 earthquake did not release the entirety of the available slip budget and that some residual slip was left behind and used by the 2025 rupture.

Understanding the Observations from SWOT and implications for hydrodynamics

The use of satellite derived observations of sea surface heights for tsunamis has been limited by the spatial resolution of the traditional altimetry satellites. The ocean signal from the 2004 M9.1 Sumatra event was retrieved from Jason-1 and ENVISAT tracks; however, the data processing for this was not trivial and the signal to noise ratio was low despite the very large magnitude (Gower, 2005; Song et al., 2005). The new generation SWOT-satellite has greatly improved those capabilities, including additional bands, revealing intriguing details of the tsunami. Figure 3a clearly shows the tsunami front (c.a. 43°N) and how the tsunami main beam propagates south-east, whereas the SWOT ascending trajectory is towards the NNE.

The time history of the tsunami-wave amplitude along the nadir track (the center of the SWOT track), resulting from our simulation, is shown in Figure 4a. A contrasting pattern can be observed in the waveforms between northern and southern latitudes. South of 47°N the tsunami propagates nearly undisrupted into the deep basin along the main tsunami beam (Figure 5) and the waveforms show a single large pulse. For higher latitudes, where the bathymetry is more complex and several topographic features that can scatter the tsunami waves are present, the wavefront splits into several pulses and the waveforms show several arrivals in each location. In the SWOT track, the same pattern can be observed, with a single and high amplitude wavefront in the southern section of the SWOT track but multiple, lower amplitude wavefronts in the northern section.

Somewhat surprisingly, dispersion is important to explain features in the SWOT track behind the main tsunami front. For tsunamis generated by large subduction earthquakes, the dominant wavelengths are so much greater than the ocean depth that, in this long-wave regime, the SWE typically provide an accurate-enough description of the tsunami; dispersive effects are usually considered minimal (Glimsdal et al., 2013). However, here we observed that the wave train behind the main front (Figure 3a) is not at all explained properly by the pure SWE solution in Figure 3b. When dispersive terms are allowed (Figure 3c) the comparison, while still not perfect, is much better. One likely explanation is that interactions between the tsunami, at its origin, with the complex bathymetry of the trench and continental slope, and with the near-source coastline, generates shorter-wavelength features which propagate out to the open ocean and require dispersion to be modeled correctly.

Implications for Hazards

The 2025 Kamchatka earthquake underscores the continuing hazard posed by great megathrust ruptures along the Kuril–Kamchatka margin. Although slightly smaller in magnitude than the 1952 M9.0 earthquake, the M8.8 event re-ruptured a large portion of the same segment and demonstrated that this margin can repeatedly generate earthquakes in the “great” class on timescales of only seven decades. That such a large rupture could recur in less than a century is a cautionary signal for seismic hazard models, which often assume centennial or longer recurrence intervals for the largest events. The implication is that strain release in 1952 was incomplete, with the 2025 rupture consuming residual slip that remained. This raises the prospect that even large ruptures may not exhaust the seismic

potential of a megathrust, leaving behind hazardous asperities capable of generating future great events.

From a tsunami hazard perspective, the comparison of 2025 and 1952 (Figure 5) is particularly striking. While the 1952 rupture included significant shallow, near-trench slip that generated a catastrophic trans-Pacific tsunami, the 2025 event ruptured further downdip and produced a smaller, although still ocean-basin–wide, tsunami. The difference highlights how tsunami hazard is not dictated by magnitude alone but by the details of the depth distribution of slip. The 1952 event devastated Pacific coastlines with runups exceeding 15 m in Kamchatka and damaging waves across the Pacific Rim. In contrast, the 2025 tsunami, though widely observed, was less destructive. Still, the 2025 case shows that even without trench-breaking slip, an M8.8 event can trigger mass coastal evacuations across multiple nations and impose major societal costs.

Together, these events emphasize two key points for hazard science and risk mitigation. First, recurrence of great earthquakes on sub-century timescales cannot be ruled out in fast-converging margins, which challenges overly-simplistic views of the seismic cycle. Second, tsunami hazard is highly sensitive to rupture style. Deep-slipping ruptures may produce relatively modest waves, but shallow trench-breaching ruptures remain the primary concern for catastrophic trans-oceanic tsunamis. For communities around the Pacific, the lesson is clear: preparedness and warning systems must assume both recurrence and variability in rupture style, since either outcome carries profound implications for regional and global tsunami risk.

Future Uses of Satellite Altimetry

Satellite observations, particularly from the SWOT era, hold significant promise for advancing tsunami science. At present, their utility for real-time forecasting or early-warning remains limited because fully processed SWOT data may take 5–10 days to be released, depending on orbital cycle. Despite this latency, the 2025 Kamchatka event demonstrates the unique value of satellite altimetry for post-event analysis. The SWOT observations provided an unprecedented view of tsunami propagation and revealed the complexity of waveforms at scales that traditional altimeters could not resolve.

These measurements offer a new pathway for improving tsunami forecasting and nowcasting. Even if not yet available in real time, SWOT-class altimetry can be assimilated

into models soon after events to refine hazard assessments during ongoing response operations. Beyond immediate applications, the dense spatial sampling allows for detailed study of tsunami hydrodynamics, including dispersion, scattering, and resonance effects that are often poorly constrained by point measurements. Such insights improve both physical understanding of tsunami behavior and the realism of numerical models that underpin hazard forecasts.

Although *in-situ* validation in our study area is limited, the close agreement between SWOT and DART observations provides confidence in the robustness of satellite altimetry for tsunami applications. Future swath altimetry missions with 2-dimensional resolution, that reduce data latency or expand spatial coverage could make space-based altimetry a critical complement to in-ocean and coastal monitoring systems, enhancing both operational response and scientific investigation of complex tsunami processes.

CONCLUSIONS

The 2025 Mw 8.8 Kamchatka earthquake and tsunami demonstrate both the hazard potential of repeated great ruptures and the scientific value of new observational tools. The event likely re-ruptured portions of the 1952 rupture zone but with slip concentrated farther downdip, producing a smaller tsunami despite its large magnitude. This underscores how rupture style, not magnitude alone, controls tsunami impact. SWOT altimetry provided the first dense spaceborne observations of a great tsunami's wavefield, validating source models against DART data and revealing complex propagation features, which are not completely resolved with current numerical models and leaves room for improving their skills based on unique set of observations. These results highlight the need to consider both recurrence and variability in rupture behavior when assessing hazard and point to the emerging role of satellite altimetry in refining tsunami forecasts and advancing our physical understanding of tsunami dynamics.

ACKNOWLEDGEMENTS

We thank Randy LeVeque, Ignacio Sepulveda, Vassily Titov, Yong Wei, Dailin Wang, Nathan Becker, Jorge Macias, Finn Lovholt, and Steven Gibbons for helpful discussions. DM received partial funding for this research from NASA grants #80NSSC23K1326 and #80NSSC22K0458, and NSF grants EAR-2225286 and OCE-2325310

DATA AND RESOURCES

All data and modeling codes used in this work are open source used in this work are open source. HYPERLINK "DART buoy data is available for download at https://catalog.data.gov/dataset/deep-ocean-assessment-and-reporting-of-tsunamis-dartr1". SWOT altimetry data is available at the Aviso repository from CNES (https://www.aviso.altimetry.fr/en/data/products/sea-surface-height-products/global/swot-l3-ocean-products.html). Bathymetry from SRTM15+ is available at https://portal.opentopography.org/raster?opentopoID=OTSRTM.122019.4326.1.The GeoClaw software is available from the developers at https://www.clawpack.org/geoclaw.

DECLARATION OF CONFLICT OF INTEREST

The authors declare that they have no competing interests.

REFERENCES

Argus, D. F., Gordon, R. G., & DeMets, C. (2011). Geologically current motion of 56 plates relative to the no-net-rotation reference frame. *Geochemistry, Geophysics, Geosystems*, *12*(11).

AVISO/DUACS: SWOT Level-3 SSH Basic (v2.0.1) [Data set], AVISO/DUACS [data set], https://doi.org/10.24400/527896/A01-2023.017, 2023a. a

Berger, M.J. & LeVeque, R.J. (2023) Implicit Adaptive Mesh Refinement for Dispersive Tsunami Propagation *SIAM J. Sci. Comput.* 46 (2024) pp. B554 - B578.

Bürgmann, R., Kogan, M. G., Steblov, G. M., Hilley, G., Levin, V. E., & Apel, E. (2005). Interseismic coupling and asperity distribution along the Kamchatka subduction zone. *Journal of Geophysical Research: Solid Earth*, *110*(B7).

Clawpack Development Team (2024), Clawpack Version 5.11.0, http://www.clawpack.org, doi: 10.5281/zenodo.13376470

Coadou-Chaventon, S., Swart, S., Novelli, G., & Speich, S. (2025). Resolving sharper fronts of the Agulhas Current Retroflection using SWOT altimetry. Geophysical Research Letters, 52(9), e2025GL115203.

Dibarboure, G., Anadon, C., Briol, F., Cadier, E., Chevrier, R., Delepoulle, A., ... & Ubelmann, C. (2025). Blending 2D topography images from the Surface Water and Ocean Topography

(SWOT) mission into the altimeter constellation with the Level-3 multi-mission Data Unification and Altimeter Combination System (DUACS). Ocean Science, 21(1), 283-323.

Glimsdal, S., Pedersen, G. K., Harbitz, C. B., & Løvholt, F. (2013). Dispersion of tsunamis: does it really matter? *Natural hazards and earth system sciences*, *13*(6), 1507-1526.

Goldberg, D. E., Koch, P., Melgar, D., Riquelme, S., & Yeck, W. L. (2022). Beyond the teleseism: Introducing regional seismic and geodetic data into routine USGS finite-fault modeling. *Seismological Society of America*, *93*(6), 3308-3323.

J. Gower (2005). Jason 1 detects the 26 December 2004 tsunami**.** *EOS Trans. Am. Geophys. Union* ***86***, 37.

Gusman, A. R., Mulia, I. E., Satake, K., Watada, S., Heidarzadeh, M., & Sheehan, A. F. (2016). Estimate of tsunami source using optimized unit sources and including dispersion effects during tsunami propagation: The 2012 Haida Gwaii earthquake. *Geophysical Research Letters*, *43*(18), 9819-982

Hutchinson, R. O. (1954). The Kamchatka earthquakes of November, 1952. *Earthq. Notes*, *25*(3-4), 37-41.

Johnson, J. M., and K. Satake (1999). Asperity distribution of the 1952 great Kamchatka earthquake and its relation to future earthquake potential in Kamchatka, Pure Appl. Geophys 154, no. 3/4, 541–553.

Kaistrenko, V., & Sedaeva, V. (2001). 1952 North Kuril tsunami: New data from archives. In *Tsunami research at the end of a critical decade* (pp. 91-102). Dordrecht: Springer Netherlands.

Koulakov, I. Y., Dobretsov, N. L., Bushenkova, N. A., & Yakovlev, A. V. (2011). Slab shape in subduction zones beneath the Kurile–Kamchatka and Aleutian arcs based on regional tomography results. *Russian Geology and Geophysics*, *52*(6), 650-667.

Lin, J. T., Aslam, K. S., Thomas, A. M., & Melgar, D. (2020). Overlapping regions of coseismic and transient slow slip on the Hawaiian décollement. *Earth and Planetary Science Letters*, *544*, 116353.

MacInnes, B. T., Weiss, R., Bourgeois, J., & Pinegina, T. K. (2010). Slip distribution of the 1952 Kamchatka great earthquake based on near-field tsunami deposits and historical records. *Bulletin of the Seismological Society of America*, *100*(4), 1695-1709.

Melgar, D., & Bock, Y. (2013). Near-field tsunami models with rapid earthquake source inversions from land-and ocean-based observations: The potential for forecast and warning. *Journal of Geophysical Research: Solid Earth*, *118*(11), 5939-5955.

Morrow, R., Fu, L. L., Ardhuin, F., Benkiran, M., Chapron, B., Cosme, E., ... & Zaron, E. D. (2019). Global observations of fine-scale ocean surface topography with the surface water and ocean topography (SWOT) mission. Frontiers in Marine Science, 6, 232.

Mungov, G., Eblé, M., & Bouchard, R. (2013). DART® tsunameter retrospective and real-time data: A reflection on 10 years of processing in support of tsunami research and operations. *Pure and Applied Geophysics*, *170*(9), 1369-1384.

Pasyanos, M. E., Masters, T. G., Laske, G., & Ma, Z. (2014). LITHO1. 0: An updated crust and lithospheric model of the Earth. *Journal of Geophysical Research: Solid Earth*, *119*(3), 2153-2173.

Prytkov, A. S., Vasilenko, N. F., & Frolov, D. I. (2017). Recent geodynamics of the Kuril subduction zone. *Russian Journal of Pacific Geology*, *11*(1), 19-24.

Santellanes, S., Goldberg, D., Koch, P., Melgar, D., Yeck, W., Crowell, B., & Lin, J. T. (2025). An unexplained tsunami: Was there megathrust slip during the 2020 Mw7. 6 Sand Point, Alaska, earthquake?. *Seismica*, *4*(1).

Song, Y. T., Ji, C., Fu, L. L., Zlotnicki, V., Shum, C. K., Yi, Y., & Hjorleifsdottir, V. (2005). The 26 December 2004 tsunami source estimated from satellite radar altimetry and seismic waves. *Geophysical research letters*, *32*(20).

Tozer, B., Sandwell, D. T., Smith, W. H., Olson, C., Beale, J. R., & Wessel, P. (2019). Global bathymetry and topography at 15 arc sec: SRTM15+. *Earth and space science*, *6*(10), 1847-1864.

Tranchant, Y. T., Legresy, B., Foppert, A., Pena-Molino, B., & Phillips, H. E. (2025). SWOT reveals fine-scale balanced motions and dispersion properties in the Antarctic Circumpolar Current. Authorea Preprints

U.S. Geological Survey (USGS) Earthquake Hazards Program (2017). Advanced National Seismic System (ANSS) comprehensive catalog of earthquake events and products, U.S. Geol. Surv. Data Release, doi: 10.5066/F7MS3QZH

Wang, J., Lucas, A. J., Stalin, S., Lankhorst, M., Send, U., Schofield, O., ... & Fu, L. L. (2025). SWOT mission validation of sea surface height measurements at sub-100 km scales. Geophysical Research Letters, 52(11), e2025GL114936.

Wirth, E. A., Sahakian, V. J., Wallace, L. M., & Melnick, D. (2022). The occurrence and hazards of great subduction zone earthquakes. *Nature Reviews Earth & Environment*, *3*(2), 125-140.

FULL MAILING ADDRESS FOR CORRESPONDING AUTHOR

Angel Ruiz-Angulo

Institute of Earth Sciences, University of Iceland.

Askja, Sturlugata 7, 102 Reykjavík, Iceland.

LIST OF FIGURE CAPTIONS

Figure 1. *Regional context for the M8.8 Kamchatka, Russia earthquake and tsunami. The star is the event hypocenter, and the focal mechanism is from the W-Phase solution, both produced by the U.S. Geological Survey (USGS 2017). Color mapping shows the sea surface height from the tsunami model otuput at 70 mins after OT (Origin Time). SWOT-derived sea surface height measured on 30-07-2025 (00:35 – 00:39 UTC) is superimposed and the satellite's flight direction is shown by the arrow. Crosses indicate the satellite's position at different times after earthquake origin. The best fitting initial sea-surface condition is shown in contours spaced 1 m apart, maroon contours represent uplift and pink contours are subsidence. The* locations of the three DART buoys (yellow triangles) used for inversion are shown as well. Bathymetry contours at 1000 m intervals are shown in light gray.

Figure 2. *(a) Vertical coseismic deformation from– the USGS version 3 finite fault model in solid colors compared to our best fitting inversion from DART data shown in contours. Bathymetry shown as 1000 m contours in light grey(b) Same as (a) but the inversion is in solid colros and the USGS model in contours. (c) Blended model consiting of the uplift from (b) with the subsidence from (a). (d) Comparison between the blended model of (c) and the deofrmation from the JASmod7 slip model for the 1952 M9 earthquake from MacInnes et al (2010)*

Figure 3. *(a) SWOT observations of sea surface height. Locations of DART buoys shown in yellow triangles. Crosses are spaced 1 min apart as in Figure 1. Bathymetry contours at 1000 m spacing shown in light gray. (b) Same as in (a) but showing the synthetic SWOT track resulting from the blended model in Figure 2. (c) Comparison of the observed and synthetic sea-surface height anomalies along the satellite's near-nadir. Grey shaded regions indicate the one-sigma uncertainty in the observations. (d) Fits to the DART observations (all locations in Figure 1) from the USGS V3 slip model, our best fitting Gaussian inversion, and the blended model. Yellow shaded regions indicate the portions of the waveform used for inversion.*

Figure 4. (*a) Timeseries of normalized synthetic tide gauges along the SWOT Nadir track for the real SWOT pass (black dots) showing the waveforms of the propagating tsunami wave. The wave is undisrupted for the lower latitudes, 41N-47N, and shows complex wave forms for higher latitudes. The band between 46-50N shows the combination of pure propagation plus dispersive bands observed in SWOT. (b) SRTM15 high resolution bathymetry showing the SWOT nadir track (black) and two representative trajectories (purple and peach), with their corresponding bathymetry shown in the same color above (purple) and below (peach).*

Figure 5. *(a) Maximum modeled tsunami amplitudes for the 2025 M8.8 earthquake (η_{2025}). (b) Maximum modeled tsunami amplitudes for the 1952 M9.0 earthquake (η_{1952}). (c) Difference shown as the natural log of the ratio of 1952 to 2025 amplitudes such that +1 corresponds to the 1952 event being a factor of e larger and -1 the 2025 event being a factor of e larger. In all panels the yellow star is the event hypocenter, 2025 SWOT track is shown as well.*

FIGURES

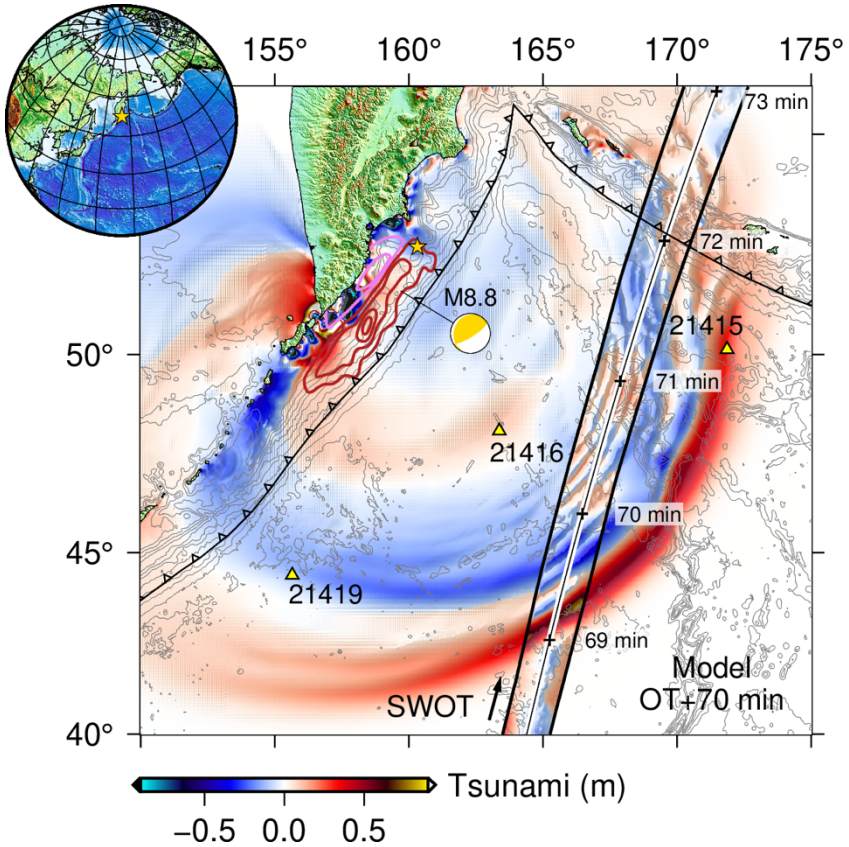

Figure 1. *Regional context for the M8.8 Kamchatka, Russia earthquake and tsunami. The star is the event hypocenter, and the focal mechanism is from the W-Phase solution, both produced by the U.S. Geological Survey (USGS 2017). Color mapping shows the sea surface height from the tsunami model otuput at 70 mins after OT (Origin Time). SWOT-derived sea surface height measured on 30-07-2025 (00:35 – 00:39 UTC) is superimposed and the satellite's flight direction is shown by the arrow. Crosses indicate the satellite's position at different times after earthquake origin. The best fitting initial sea-surface condition is shown in contours spaced 1 m apart, maroon contours represent uplift and pink contours are subsidence. The locations of the three DART buoys (yellow triangles) used for inversion are shown as well. Bathymetry contours at 1000 m intervals are shown in light gray.*

Alt-text: *Map of the 1952 M8.8 Kamchatka earthquake and tsunami showing the hypocenter, focal mechanism, modeled and SWOT-measured sea surface heights, satellite track and timing, initial uplift and subsidence contours, three DART buoy locations, and bathymetry contours.*

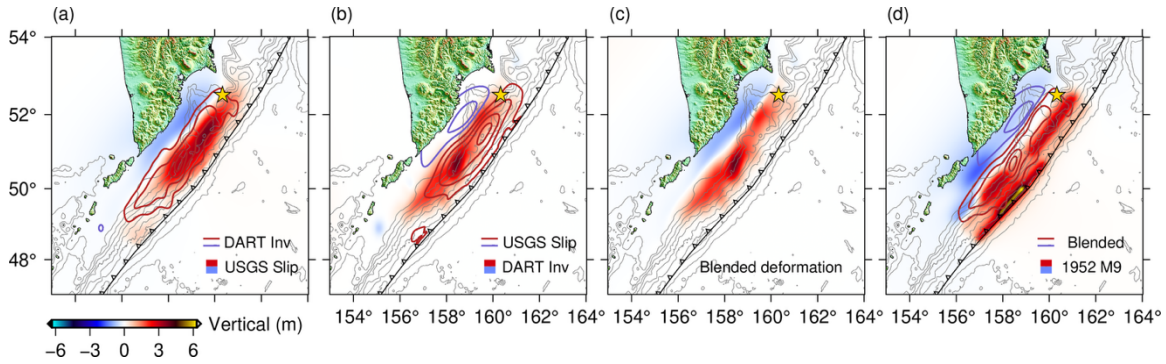

Figure 2. *(a) Vertical coseismic deformation from– the USGS version 3 finite fault model in solid colors compared to our best fitting inversion from DART data shown in contours. Bathymetry shown as 1000 m contours in light grey(b) Same as (a) but the inversion is in solid colros and the USGS model in contours. (c) Blended model consiting of the uplift from (b) with the subsidence from (a). (d) Comparison between the blended model of (c) and the deofrmation from the JASmod7 slip model for the 1952 M9 earthquake from MacInnes et al (2010)*

Alt-txt: *Panels compare vertical coseismic deformation for the 1952 M9 Kamchatka earthquake: USGS finite fault model versus DART inversion, shown in solid colors and contours; a blended model combining uplift and subsidence; and comparison of the blended result with the JASmod7 slip model.*

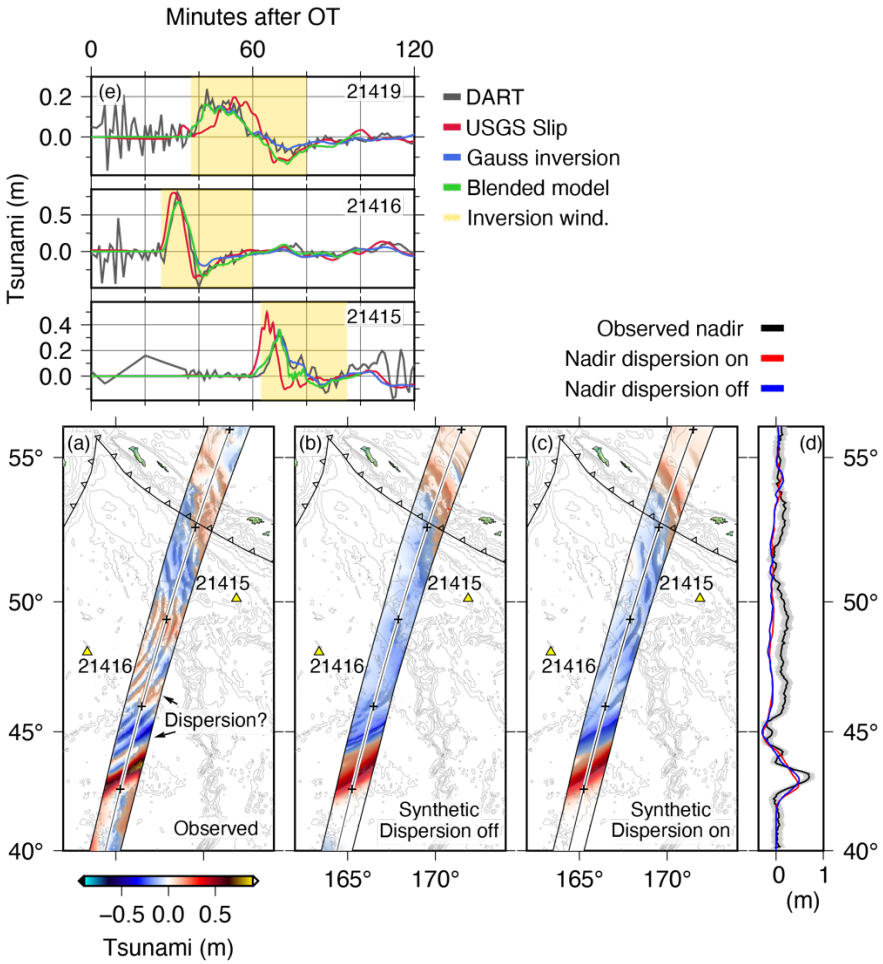

Figure 3. *(a) SWOT observations of sea surface height. Locations of DART buoys shown in yellow triangles. Crosses are spaced 1 min apart as in Figure 1. Bathymetry contours at 1000 m spacing shown in light gray. (b) Same as in (a) but showing the synthetic SWOT track resulting from the blended model in Figure 2. (c) Comparison of the observed and synthetic sea-surface height anomalies along the satellite's near-nadir. Grey shaded regions indicate the one-sigma uncertainty in the observations. (d) Fits to the DART observations (all locations in Figure 1) from the USGS V3 slip model, our best fitting Gaussian inversion, and the blended model. Yellow shaded regions indicate the portions of the waveform used for inversion.*

Alt-txt: *Panels compare SWOT and model results for the 1952 Kamchatka tsunami: observed sea surface heights with DART buoy locations, synthetic SWOT track from the blended model, cross-track comparison of observed and modeled height anomalies with uncertainties, and DART waveform fits from different slip and inversion models highlighting the data segments used.*

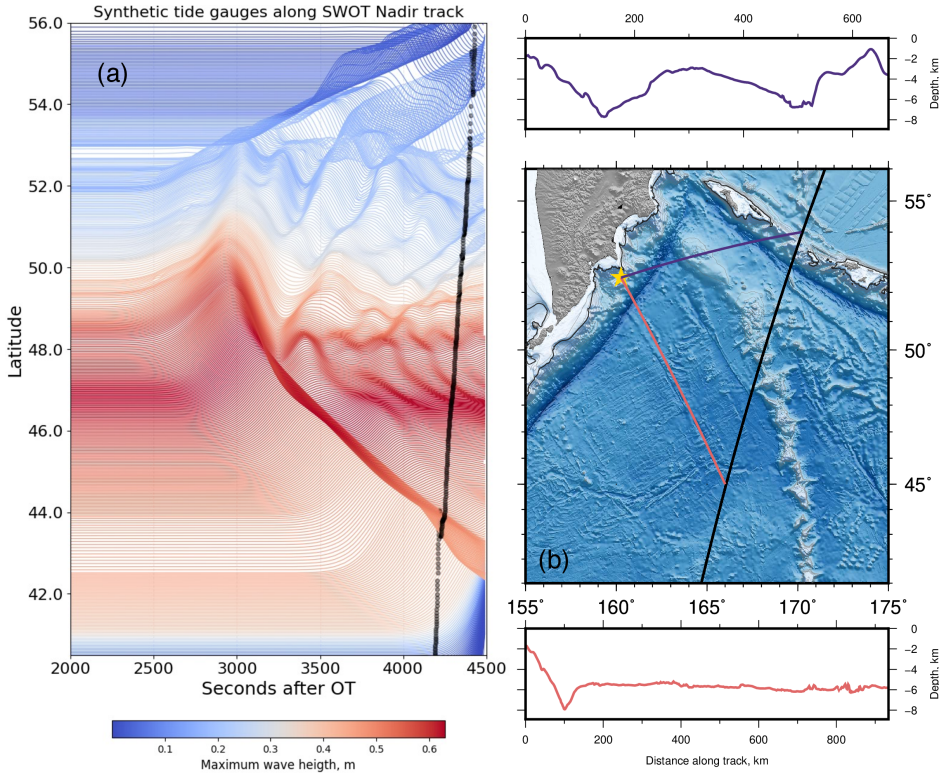

Figure 4. (*a) Timeseries of normalized synthetic tide gauges along the SWOT Nadir track for the real SWOT pass (black dots) showing the waveforms of the propagating tsunami wave. The wave is undisrupted for the lower latitudes, 41N-47N, and shows complex wave forms for higher latitudes. The band between 46-50N shows the combination of pure propagation plus dispersive bands observed in SWOT. (b) SRTM15 high resolution bathymetry showing the SWOT nadir track (black) and two representative trajectories (purple and peach), with their corresponding bathymetry shown in the same color above (purple) and below (peach).*

Alt-txt. *Time series of synthetic tide gauges along the SWOT track showing tsunami waveforms, simple at lower latitudes and increasingly complex with dispersive features north of 46°N, together with high-resolution bathymetry along the track and two representative cross-sections.*

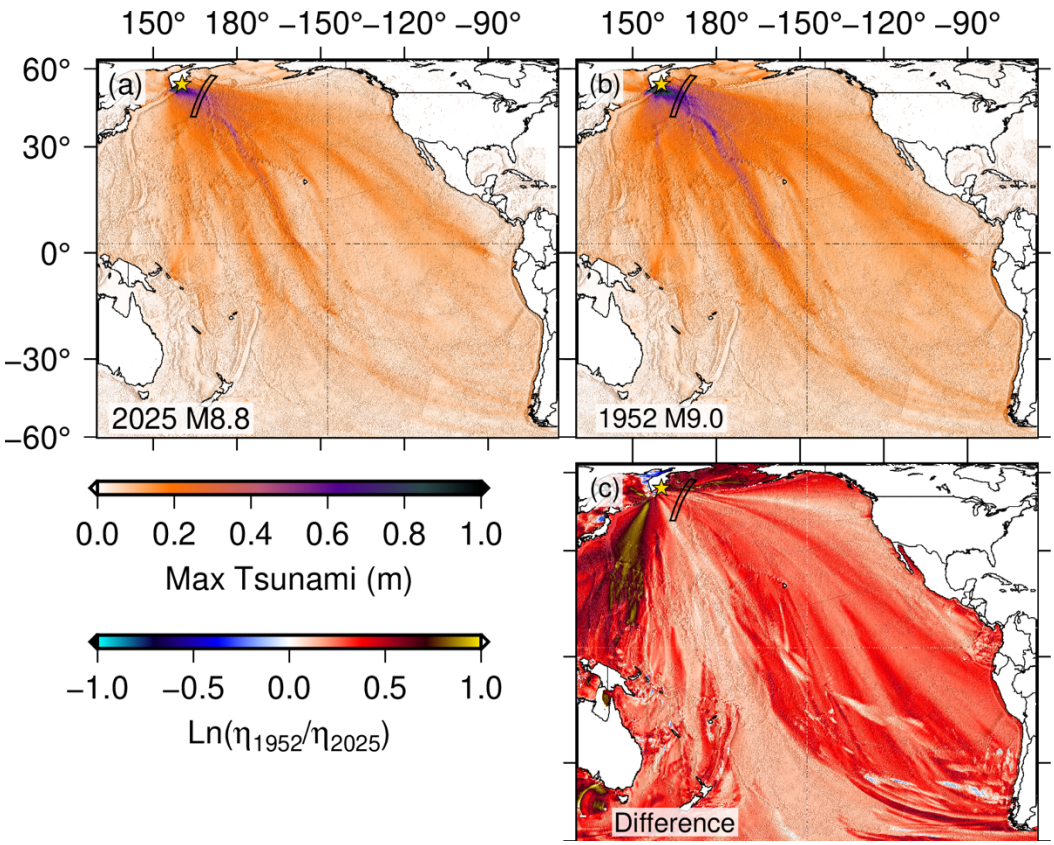

Figure 5. *(a) Maximum modeled tsunami amplitudes for the 2025 M8.8 earthquake (η_{2025}). (b) Maximum modeled tsunami amplitudes for the 1952 M9.0 earthquake (η_{1952}). (c) Difference shown as the natural log of the ratio of 1952 to 2025 amplitudes such that +1 corresponds to the 1952 event being a factor of e larger and -1 the 2025 event being a factor of e larger. In all panels the yellow star is the event hypocenter, 2025 SWOT track is shown as well.*

Alt-txt: *Maps of maximum modeled tsunami amplitudes for the 2025 M8.8 and 1952 M9.0 Kamchatka earthquakes, with a third panel showing the logarithmic ratio of the two. Hypocenters are marked with yellow stars and the 2025 SWOT satellite track is included.*